Sub-Picosecond Non-Equilibrium States in the Amorphous Phase of GeTe Phase-Change Material Thin Films

Paloma Martinez, Valérie Blanchet, Jérôme Gaudin, Dominique Descamps, Jean-Baptiste Dory, Claude Fourment, Irène Papagiannouli, Stéphane Petit, Jean-Yves Raty, Pierre Noé

Sub-Picosecond Non-Equilibrium States in the Amorphous Phase of GeTe Phase-Change Materials Thin Films

Paloma Martinez, Valérie Blanchet, Dominique Descamps, Jean-Baptiste Dory, Claude Fourment, Irène Papagiannouli, Stéphane Petit, Jean-Yves Raty,* Pierre Noé,* Jérôme Gaudin**

P. Martinez, Dr. J. Gaudin, Dr. I. Papagiannouli, Dr. D. Descamps, Dr. S. Petit, Dr. V. Blanchet, Dr. C. Fourment
CELIA, Université Bordeaux, CEA, CNRS, UMR 5107, 351 Cours de la Libération, F-33405 Talence, France
Email Address: paloma.martinez@u-bordeaux.fr; jerome.gaudin@u-bordeaux.fr
Dr. C. Fourment
CEA-DAM-CESTA, F-33114 Le Barp, France
Dr. J.-B. Dory, Dr. J.-Y. Raty, Dr. P. Noé
Université Grenoble Alpes, CEA, LETI, 17 rue des Martyrs, F-38000 Grenoble Cedex 9, France
Email Address: pierre.noe@cea.fr
Dr. J.-Y. Raty
FRS-FNRS and CESAM, University of Liège, Allée du 6 Août 19, 4000 Sart-Tilman, Belgium
Email address: jyraty@uliege.be

Keywords: *chalcogenide, ovonic threshold switching, fast transition, amorphous, GeTe*

The sub-picosecond response of amorphous Germanium Telluride thin film to a femtosecond laser excitation is investigated using frequency domain interferometry and *ab initio* molecular dynamics. The time-resolved measurement of surface dynamics reveals a shrinkage of the film with a dielectric properties response faster than 300 fs. The systematic *ab initio* molecular dynamics simulations in non-equilibrium conditions allow us to retrieve the atomic configurations for ionic temperature from 300 K to 1100 K and width of the electron distribution from 0.001 eV to 1.0 eV. Local order of the structures is characterized by in-depth analysis of the angle distribution, phonon modes and pair distribution function which evidence a transition towards a new amorphous electronic excited state close in bonding/structure to the liquid state. Our results shed a new light on the optically highly excited states in chalcogenide materials involved in both important processes: phase-change materials in memory device and Ovonic threshold switching phenomenon induced by static field.

In 1968, Stanford R. Ovshinsky discovered the ability of some glassy semiconductors to switch rapidly and reversibly between a highly resistive and a conductive state upon application of a high electric field. [1] Besides, Ovshinsky divided these amorphous chalcogenide compounds into two categories depending on whether they are able to remain in the highly conducting state when the electrical current is switched off. The first class, commonly based on Te, named 'phase-change materials' (PCM) switches easily to the conductive state thanks to their rapid crystallization kinetics, that is orders of magnitude faster than in regular chalcogenides. The second category is that of 'Ovonic threshold switching' (OTS) materials, recovering a highly resistive amorphous phase after being switched to the conductive state.
In both PCM and OTS materials, the threshold switching (TS) mechanism occurring in the amorphous phase upon high electrical field application is the key mechanism allowing their use for memory applications. Indeed, as the TS mechanism in OTS materials allowed achievement of OTS selector devices, the same TS process occurring in the amorphous phase of PCM is behind their use in non-volatile resistive memory cells. In an OTS selector device, the TS enables the reversible transition between a highly resistive state (OFF state) and a conductive state (ON state) when the voltage applied on the OTS chalcogenide glassy thin film exceeds a critical threshold value, V_{th}. [1,2]Then, when the current is reduced below the holding current density, J_h, the OTS selector recovers its high resistance state and always remains amorphous. [1] In a resistive PCM memory device, the huge contrast of resistivity between a high resistance state (RESET)

corresponding to the amorphous phase of PCM and the low resistance state (SET) of its crystalline counterpart is used to binary code the information between 0 and 1. The reversible transition between both states is obtained by Joule heating of the PCM by means of application of current pulses with varying amplitude and duration. [3] We emphasize that similarly to OTS materials the same TS process is a key process in the amorphous phase of PCM. Indeed, the PCM memory cell is programmed in the RESET state through a melt-quench process of the crystalline phase by means of application of intense and short electrical pulses. In the RESET amorphous state, the Joule heating effect is limited, since current passing through the PCM is very low due to the very high resistance of PCM amorphous phase. Then, similarly to OTS glass suddenly at V_{th} the amorphous phase becomes highly conductive, thus enabling more efficient Joule heating. Therefore, the PCM memory cell is programmed to the SET state by means of electric pulses applied at voltage beyond V_{th} voltage but with a limitation of current intensity. Finally, the thermal stress applied to the memory cell is then properly controlled by pulse duration and the value of the current compliance, thus allowing the crystallization or the amorphization of the PCM. In both OTS and PCM chalcogenides, TS is the same physical mechanism but with two main differences between both being the value of V_{th} and the ability of the material to crystallize or not after TS.
To date, the discovery of such original materials led to a wide range of applications, the most successful ones being in non-volatile phase-change memories (PCM memory) [3,4] and as OTS selector devices for 3D resistive memory arrays. [2,5–8] In both PCM and OTS materials, the typical time scale for a threshold switching of the amorphous phase is the nanoseconds scale. In PCM memory, the threshold switching comes prior to the slightly slower, but still measured in nanosecond range, electrically-induced transition to the stable conductive crystalline state. The transition can be quasi-infinitely reversible thanks to the possible re-amorphization of the crystalline phase by a simple, fast-enough, melting-quenching under an intense electrical or laser pulse. [6,9]

In both OTS and PCM materials, the phase transition is linked to a change of the local order which is responsible for the huge modification of the macroscopic physical properties. [2,10] Investigating the changes of local order induced by different stimuli (thermal, [11] electric field, [12] pressure, [13,14] photons [15,16]) is of high practical importance to garner hitherto unavailable insights into OTS mechanism and phase transition in PCMs. As the atomic dynamic is taking place in the femtosecond regime, ultra-fast experimental techniques are particularly suited to harvest valuable insights. Most of the previous studies were devoted to the crystalline materials, investigated by time-resolved diffraction experiments with femtosecond x-ray or electron sources. [17,18] Diffraction techniques are sensitive to the long range order and as a consequence, maybe not the best suited tools to investigate local order dynamics, especially in the amorphous phase. Most of the experimental approaches are based on a femtosecond light pulse triggering the change of local order, leading to a specific non-equilibrium condition where the lattice and the electron temperatures are not equal: $T_i \neq T_e$. Above a certain threshold, this can result in a so called non-thermal phase transition, a well known process in semi-conductors, [19] also evidenced in common PCMs such as $Ge_2Sb_2Te_5$. [17] In that material, as in GeTe, studies have suggested that the change of order was driven by some rattling motions of Ge atoms, [20] resulting in a loss of resonant bonding and finally to the amorphization of the material. On the contrary, all-optical experiments performed by Miller *et al.* [21] lead to the conclusion that the Te atoms were driving the phase transition. The common observation to all these experiments is the pronounced phonon softening [22]. Markedly fewer experiments were performed on the amorphous phase of these materials besides the debated direct amorphous-to-crystalline phase transition observed in GeSb [23,24] Most of the experiments were backed by *ab initio* molecular dynamics (AIMD) simulations performed on the pristine materials in their initial state but very few on the excited ones. These AIMD studies showed that the local environments in the crystalline and the amorphous phase of PCM are very close in structure. Recently, the metavalent bonding concept (MVB) [25–27] was introduced to describe the unique bonding characteristics of crystalline phase of PCMs. MVB differs from the previously proposed model of resonant bonding, initially describing graphene and aromatic molecules, as MVB results in a high chemical bond polarizability as well as uncommon vibrational properties such as unusual phonon softening and large Grüneisen parameters. [25–27] MVB is therefore at the origin of the portfolio of outstanding properties of PCMs such as the huge and uncommon increase of electronic conductivity and polarizability upon

crystallization. Kolobov *et al.* [28] simulated the non-thermal amorphous to crystal transition of $Ge_2Sb_2Te_5$ but once again, studies on the amorphous material are scarse and even the structure of the pristine material is still highly debated and controversed. [29–31]

The overall picture can be summarized as follows: non-thermal phase transition can be triggered in PCM materials but the atomistic dynamics and electronic excitation inherent to such transition remain largely elusive. The link between PCM phase transition and OTS mechanism roots in the electronic excitation that drives the system in the non-equilibrium conditions (induced by the light pulse in the aforementioned references). [2] As a result, triggering of phase-transition and threshold switching with a femtosecond light pulse seems pertinent. Finally, this non-exhaustive summary of previous studies leaves some open questions: What are the changes in the local structure in terms of bond angles, length and nature induced by the electronic excitation? Does the non-thermal transition lead to a direct solid to solid pathway, or is a transient liquid state involved?
Designing material with shorter switching time for enticing devices and applications, requires to determine what is the effect of the electronic excitation on nuclei motions: which ones are moving and which are the most relevant ones that will define the transient and final structural phase. The challenges are multiple with a determination of the rise in temperature of electrons and how does its amplitude depend on the laser fluence (i.e. the electronic excitation). This demands an intimate understanding of phase-change on the microscopic level, meanwhile the experimental approach requires a very strict control of the macroscopic state of the sample to avoid emergence of a detrimental desorbed gaz or plasma. GeTe is a material of choice to study these topics, being a prototypical phase-change material, but also an excellent thermoelectric [32] and a promising material for spin-orbitronics. [33] Besides, GeTe is easier to simulate than $Ge_2Sb_2Te_5$ alloy due to its simpler binary composition, and yet with a real potential in data storage memory applications compared to the other Ge-Sb-Te compounds lying on the GeTe-Sb_2Te_3 tie-line of the Ge-Sb-Te ternary phase diagram, thanks to its very high crystallization rate enabling very fast PCM memory devices. [34]
In the present study, we investigate by frequency-domain interferometry (FDI) the dynamics in electronic excited amorphous GeTe thin films during the first picoseconds following a 26-fs pulse excitation at different fluences. Extensive *ab initio* molecular dynamics simulations over a wide range of T_e and T_i are performed resulting in transient structures defined as non-equilibrium states. In depth analysis of these structures enables to monitor the change of the local structure and build-up a molecular movie of the electronic excitation effect over the first 9 ps timescale with a sub 100 fs time resolution. In the case of the experiment with the amorphous phase as pristine material, two final phases are possible: the crystal or another disordered phase. The final state is mainly dependent on the cooling rate conditions enabling or not the "quenching" of the liquid phase obtained after material melting. The initial step is the same for both cases, and the subject we will investigate in our contribution.

Pristine amorphous thin films of GeTe deposited by industrial magnetron sputtering, either capped *in situ* with a protective SiN layer (see the Experimental section) or left uncapped, were studied by means of a pump-probe technique combining frequency-domain interferometry. [35–37] The detailed experimental set-up is depicted in **Figure 1A** and briefly explained in the Experimental section (a complete description is provided in Reference [36])). The interference pattern of two delayed-probe pulses (central wavelength $\lambda_0 = 532\,\text{nm}$, full width at half maximum ,FWHM, duration of 120 fs) after reflection on the sample gives access to the relative variation of complex reflectivity of the sample $\delta R = r \cdot e^{i\phi}$ (r being the modulus and ϕ the phase of δR). Triggering the electronic excitation of the sample with the pump pulse (800 nm central wavelength, 26 fs FWHM duration) between those two probe pulses induces a change in R. With E_1 and E_2 the electric field of each probe pulse, the resulting E at the entrance slit of the spectrometer is given by $E = E_1 + \delta R \cdot E_2$. The Fourier transform of the total electric field yields the intensity I on the CCD camera of the spectrometer, as per **Equation 1**, with ω_0 the central angular frequency of the probe and δt the fixed delay between the two probe pulses (8.7 ps in our setup).

$$I(\omega, \delta t) = I_0(\omega)\left(1 + r^2 + 2r \cdot cos(\phi - \omega_0 \delta t)\right) \quad (1)$$

Typical measured interferograms are shown in **Figure 1B** for S and P projection of the reflected probes

at a pump-probe delay $\Delta t = 8.5$ ps. The horizontal and vertical axes correspond to the spectral and the spatial axis, respectively. The red rectangles represent the irradiated area by the pump. In this area, the fringes are clearly shifted due to the δR induced at t=0 by the pump pulse. Their visibility is modified compared to the non-irradiated top and bottom area, as a result of the pump irradiation.

The simultaneous measurement of R in S and P polarizations for each pump-probe delay thanks to a Wollaston prism mounted in front of the spectrometer, enables to retrieve the surface dynamics and the dielectric properties. [38] The probe beams are reflected on the surface of the sample with an incident angle $\theta = 45°$. The Fresnel **Equation 2** gives then the following relationship between the complex reflectivities in S and P polarizations (R_S and R_P, respectively) :

$$R_P = R_S^2 \Rightarrow \begin{cases} r_P/r_S^2 = 1 \\ 2\phi_S - \phi_P = 0 \end{cases} \tag{2}$$

The relations in Equation 2 are only valid for a sharp interface. As soon as deviations from these equivalencies are observed, information on the surface dynamics can be extracted such as:

- $r_P/r_S^2 \neq 1$ means that a gas or a plasma is developing.
- $2\phi_S - \phi_P \neq 0$ implies that the interface is moving. The displacement d of the surface is then given by the **Equation 3**. $d > 0$ indicates that the sample expands while $d < 0$ corresponds to shrinkage.

$$d = \lambda_0 \left(2\phi_S - \phi_P\right) / \left(4\pi \cdot cos\theta\right) \tag{3}$$

The displacement d as a function of the pump and the second probe pulse delay Δt is shown in **Figure 1C** for pump fluences from 16 to 80 mJ/cm^2. The time when the pump pulse is impinging on the sample defines the delay $\Delta t = 0$. This zero delay is determined by a direct imaging technique independant of the FDI measurement with a precision of 30 fs.

About 1 ps after the pump irradiation, the surface undergoes a negative continuous displacement for fluences greater or equal to 26 mJ/cm^2. Here the 8.7 ps of recording is restrained by the fixed delay between the two probes pulses. The ratio r_P/r_S^2 being equal to 1 for all delays and fluences, indicates that the surface of our sample stays either solid or liquid during the whole time studied (see Figure S2 the Supporting Information). We can conclude that the GeTe thin film actually shrinks due to 800 nm-laser excitation. This shrinkage is not negligible as it can reach up to 4 nm (0.8% of the film thickness) in 8.7 ps for an irradiation of 80 mJ/cm^2. At low pump fluence (<30 mJ/cm^2 no displacement of the surface is measured whether capped or uncapped GeTe sample.

The timescale of electron-phonon coupling is the picosecond. [19,39]The shrinkage which appears (for F≥26 mJ/cm^2) here is therefore either due to formation of an excited solid state or of a liquid phase of higher density. The measured shrinkage is proportional to the total volume of the excited/melted volume. As the excited volume is limited by the absorption depth of the pump, nearly 125 nm at 800 nm wavelength in our amorphous GeTe film, this would correspond to a shrinkage too small to be detected. However, the formation of fingerprints patterns observed by post-experiment phase-contrast microscopy (see the Reference [40] and Figure S3) leaves no doubt on the formation of a liquid layer for F≥26 mJ/cm^2. The volume of melted material increases with time as the front of the liquid phase propagates thanks to thermal transport, and the shrinkage becomes large enough to be detected. As a consequence, the shrinkage detected in the present experiment provides the timescale of the apparition of a molten layer. This is an upper limit fixed by the sensitivity of our set-up. One should emphasize that measurement of a negative change of volume is also indirectly observed in our *ab initio* simulations (Supporting Information, Figure S5).

Prior-irradiation ellipsometry measurements on the thin film sample in as-deposited state (dashed lines), along with our time-resolved measurement of relative variation of reflectivity enable to retrieve the time

evolution of the real (ε_r) and imaginary (ε_i) parts of the dielectric function of pristine amorphous GeTe material, as plotted in **Figure 1D**. The variation of ε_r evidences an ultrafast transition: in less than 250 fs after the pump irradiation, with a decrease from 12.66 to approximately zero. Miller *et al.* [21] obtained the similar tendencies and timescales for optical excitation of $Ge_2Sb_2Te_5$, this alloy being also a prototypical PCM. The variation of the pump fluence has no effect on the recorded transients of ε_r.
On the contrary, the imaginary part of the dielectric function is strongly influenced by the intensity of the excitation, and evolves on a different timescale than ε_r. At short times after excitation, ε_i does not vary much. However, on a longer timescale, the response is very different depending on the fluence: after 1-2 ps, ε_i increases for low fluences, but decreases for high fluences (transition around 31 mJ/cm^2). Still, the variation in the imaginary part is not much significant, even on this longer timescale. The dielectric function reveals a transition, seemingly without formation of a liquid phase (ie. a direct amorphous-amorphous transition) since no shrinkage (nor expansion) of the sample was detected for these low fluences ($< 26\,$mJ/cm^2, Figure 1C).

FDI results presented in Figure 1 clearly indicate a transition from the as-deposited GeTe to another state upon laser excitation. Since post-experiment nano-beam electron diffraction analysis within the irradiated volume of the GeTe film reveals no sign of crystallization, [40] the final state is also an amorphous state, but distinct from the initial one as evidenced by the change of refractive index shown on the optical microscope pictures (Figure S3 in the Supporting Information). To identify the origin of the underlying process behind this transition, we conducted *ab initio* molecular dynamics (AIMD) simulations.

Describing the exact structure of as-deposited amorphous GeTe is a challenging task. [41–43] In that context, among the various amorphous GeTe structural model we simulated, we chose to use as initial amorphous GeTe configuration the one that best reflects the structure of our films deposited by sputtering. [44] It differs significantly from the structures obtained by standard melt-and–quench method (for details on the amorphous GeTe model see the Experimental Section). In our model, the average coordination numbers are equal to 4.15 and 2.36 for Ge and Te atoms, respectively. About 80% of the Ge atoms are in tetrahedral sites (obtained from analysis of the ratio d_4/d_0 of the 4^{th} closest neighbour distance $d4$ around each atom and the average of the three closest ones d_0 [45]) while only 5% are in octahedral sites with a coordination number between 5 and 6. From previous literature, we expected a prevalence of the octahedral sites over the tetrahedral ones. [46,47] However, most of the literature models use a melt-quench approach that yields a smaller proportion of tetrahedra in comparison to sputter-deposited materials, as shown by Akola and Jones. [47] In our model, it is the large proportion of homopolar Ge-Ge bonds that explains this unusual ratio, inducing a gapless density of states (see Figure S4 of Supporting Information).

To model the excitation from the femtosecond pulse irradiation, we fixed the Fermi distribution of electrons with a given width σ (see Experimental section), which can be assimilated to an electronic temperature T_e. We performed a systematic constrained density functional theory (DFT) study by varying both T_e, in the range (0.001, 0.05, 0.1, 0.3, 0.5, 0.7, 0.85, 1.0) eV and the ionic temperature T_i in the range (300, 450, 600, 750, 900, 1100) K. However it is not sufficient to quantitatively compare experimental results and simulations. Indeed, DFT is known to underestimate the band gap, which affects the dielectric properties and prevents any direct comparison with the experiment. To overcome these issues, we considered relative variations (instead of absolute quantities) and compared the short timescale after laser excitation ($\leq$ 750 fs), during which the lattice is supposedly still at room temperature (300 K) with the simulations at T_i=300 K. For probe wavelengths lower than 650 nm, we get a lack of sensitivity to (T_e, T_i) variations on ε_i as shown on Figure S6 (Supporting Information), preventing us from the full investigation of the fluence dependencies of the relaxation dynamics. For now on, we focus only on the real part of the dielectric function. In **Figure 2A**, the scatter points represent the experimental relative variation of ε_r : $\left(\varepsilon_r - \varepsilon_r^{cold}\right)/\varepsilon_r^{cold}$ for each laser fluence in which ε_r^{cold} has been measured pre-irradiation by ellipsometry. On each subplot, the dotted horizontal lines correspond each to the relative variation of ε_r from simulations done at different T_e with a fixed T_i=300K. In this range of simulated electronic temperature, it appears that $T_e = 0.5$ eV is in good agreement with the asymptotic experimental value for the fluences $F \geq 26$

Table 1: Bond lengths from $g(r)$

T_i (K)	T_e (eV)	r_{Ge-Ge} (Å)	r_{Ge-Te} (Å)	r_{Te-Te} (Å)	r_{total} (Å)	method	"state"
300 K	0.001 eV	2.54	2.69	2.86	2.66	DFT	amorphous
300 K	0.5 eV	2.66	2.79		2.79	DFT	amorphous
600 K	0.3 eV	2.69	2.81		2.81	DFT	
900 K	0.1 eV	2.69	2.81		2.79	DFT	
1100 K	0.1 eV	2.69	2.81		2.81	DFT	liquid
299 K		2.479	2.649			EXAFS [53]	amorphous
300 K		2.60	2.78	2.87	2.78	DFT [43]	amorphous
300 K		2.473	2.628			EXAFS [44]	amorphous
300 K		2.48-2.50	2.66-2.70	2.89		DFT [31]	amorphous
965 K		2.57	2.74	2.91		DFT [51]	supercooled liquid
1032 K		2.57	2.74	2.93		XRD [51]	liquid
1073 K					2.72	DFT [49]	liquid

mJ/cm^2. From this agreement, we deduced five transient cases within the (T_i-T_e) pairs simulated, each representative of the relaxation of GeTe after electronic excitation, as shown in **Figure 2B**. Before the pump irradiation, the GeTe film is in its "cold" state : the ions are at room temperature, 300 K, and the electron are unperturbed (T_e = 0.001 eV). Then we pump, ie. we apply a Fermi distribution of width T_e = 0.5 eV, while the lattice is still at T_i = 300 K. Beyond $\sim$ 250 fs, the electrons and the phonon couple to give an out of equilibrium state, arbitrarily : T_i = 600 K, T_e = 0.3 eV. This exchange of energy carries on, going through the case just before the melting temperature T_m (998 K for bulk GeTe [6]) : T_i = 900 K, T_e = 0.1 eV and finally we reach an equilibrium liquid state : T_i= 1100 K, T_e = 0.1 eV.

While Figure 2B carries most of the information, it is still a challenging task to extract quantitative information about the relaxation process. It seems that the coordination number increases with T_i. For that purpose, we introduced the pair distribution function (PDF), often used to compare different structures. It represents the probability (relative to a uniform gas) to find an atom B at a distance r from an atom A. The partials and the total PDFs in **Figure 3A** are in relatively good agreement with calculations and measures done previously on amorphous GeTe. [43,44,48–56] The radii of maximum probability for each bond are summarized in **Table 1**.
For the initial state of our sample (T_i = 300 K and T_e = 0.001 eV), we find r_{Ge-Ge} = 2.54 Å while experiment by extended X-ray absorption fine structure (EXAFS) measurements, [44,53] give a length of 2.47-2.48 Å. As we compare now with other DFT, r_{Ge-Ge} is estimated to be 2.48-2.60 Å, [31,43,51] which is consistent with our value. With the same temperatures, r_{Ge-Te} is estimated at 2.69 Å, while previous studies gave 2.60-2.78 Å [31,43,44,51,53–56] and r_{Te-Te} = 2.86 Å is also in the range 2.67-2.87 Å obtained via simulations. [43]
For each type of bond, the response to electronic excitation is the same: originating from an initial atomic configuration which is structured with three peaks in the PDF (T_i = 300 K, T_e = 0.001 eV), the liquid (T_i = 1100 K, T_e = 0.1 eV) becomes characterized by much loosely defined neighbors shells. What is most interesting is the process inbetween those two configurations. In the very first moments after excitation (T_i = 300 K, T_e 0.5 eV) the bonds lengthen as shown in Figure 3A, then as electron-phonon coupling comes at play (T_i = 600 K, T_e = 0.3 eV), the inter-atomic distance stabilizes and as the material goes towards equilibrium, the values do not change much anymore. This analysis demonstrates that as soon as the electrons and phonons couple, the excited GeTe and the liquid GeTe exhibit similar bonding configuration. The diffusion coefficient D deduced from the mean square displacement (MSD) for each configuration (see Figure S9 in the Supporting Information), indicates that in all cases where $T_i \geq$ 300 K, the sample is in fact in a liquid state. In those cases, D is 30 to 200 times bigger than in the initial amorphous state, for which D_{init} is 3.2x10^{-7} cm^2/s. The excited state T_i = 300 K, T_e = 0.5 eV (encountered $\sim$ 750 fs), is an ambiguous case between an amorphous and a very viscous state. Indeed its corresponding D is 5 times bigger than D_{init}, but still very low compared to the ones expected for a pure liquid state.

Table 2: Coordination numbers. r_{cut} : cut-off radius

T_i (K)	T_e (eV)	n_{Ge}	n_{Te}	r_{cut} (Å)
300 K	0.001 eV	4.15	2.36	3.10
300 K	0.5 eV	5.25	3.42	3.35
600 K	0.3 eV	4.88	3.69	3.33
900 K	0.1 eV	5.41	4.08	3.40
1100 K	0.1 eV	7.06	6.16	3.73

The coordination numbers (CNs), as presented in **Table 2**, are determined from the PDFs curves and the cut-off radii r_{cut} of the total PDF in each case. The CNs shows an overall increase, going from the initial values of 4 and 2 for Ge and Te atoms respectively to 7 and 6 for the highest T_i state. To get more insight on the local geometries in our sample, the distribution of angles for the different temperatures discussed beforehand is represented in **Figure 3B**. In the "cold" state (T_i = 300 K, T_e = 0.001 eV), the angular distribution of each species shows one peak, centered at 104° for the Ge atoms (mostly tetrahedral environment) and 95° for the Te atoms. These values are consistent with the coordination numbers, and with those determined in simulations and experimental works. [11,43,46,57,58]
As we simulate an electronic excitation, Te and Ge atoms behave differently. The angular distribution of Te broadens. The excitation does not induce a change in geometry of the local environment of Te. On the contrary, Ge angular distribution shows a clear evolution. From the initial tetrahedral configuration, Ge geometry shifts towards an octahedral geometry with angles about 94° when it goes out of equilibrium (T_i = 600 K, T_e = 0.3 eV). Then as GeTe evolves towards the liquid state, the distribution broadens, yet the main peak of Ge remains at the same value of 94°, in agreement with previous studies on liquid GeTe. [49,51,59] As for the pair distribution function, the main modifications happen right after the excitation, in the out-of-equilibrium state. Afterwards, only small disturbances occur such as broadening of distributions, mainly due to thermal agitation.
The vibrational density of states (VDOS), represented on Figure **3C**, confirms also a negligible change for the Te curve as a function of (T_e,T_i), while the Ge one shifts drastically as soon as excitation comes up and inducing a large softening of the phonon modes. Ge atoms seem to be the key of the dynamics we observed experimentally as in the case of the crystal material. [20]

Due to the Peierls distortion mechanism, GeTe crystal is characterized by a distorted structure with the presence of alternating short and long bonds. To some extent, this pattern can be observed in disordered p-bonded semiconductors as well. [30,48,51,60–63] In order to check whether such distortions are present in our configurations, we computed the bond length correlation between two successive almost-aligned bonds, also called angular limited three-body correlation (ALTBC). **Figure 4** shows the ALTBC map of the bonding type Te-Ge-Te as previous works showed that the Peierls distortion is favored by the alternation of the species. [48,49] Additional ALTBC of the Ge and the Te atoms are given in Supporting Information (Figure S10).
The initial state is composed of a majority of tetrahedra, thus not contributing to the ALTBC which only includes contributions from bonds deviating less than 25° from the ideal aligned configuration. However the computed ALTBC does exhibit some reminiscence of Peierls distortion (Figure 4A). It shows short-long bond correlation with a maximum of correlation for (r_1,r_2)=(2.9,3.1 Å). Under electronic excitation of GeTe, the correlation pattern changes : from a "boomerang" pattern (Figure 4A), it becomes more triangular in out of equilibrium state (Figure 4B), then reshapes towards a cross pattern while becoming liquid (Figure 4C and 4D). The extension of the main peak in the antidiagonal (Figure 4A) expresses the fact that facing bonds of lengths r1 and r2 are such that r1+r2 is a constant. It would be the case in a Peierls distorted system, but also in a vibrating perfectly octahedral geometry. At T_i = 1100 K, the maximum correlation is at (r_1,r_2)=(2.9,2.9 Å) meaning that the electronic excitation leads to a uniformisation of the bond lengths, thus to a state of GeTe which does not exhibit distortion, on the contrary to previous works in which the liquid phase GeTe of same ionic temperature showed a clear Peierls effect. [48,49,51]

In conclusion, femtosecond laser irradiation of amorphous GeTe thin film induced a switching towards a different amorphous GeTe phase. Using frequency-domain interferometry we were experimentally able to follow the sample ultrafast response to the laser excitation. This response occurs on two different timescales : on a short timescale, it takes only 300 fs for the real part of the dielectric function to drop and stabilize. On a longer timescale, we observed the material shrink up to 4 nm in 9 ps for fluences of 26 mJ/cm^2 and above. While those fluences induce the formation of a liquid phase, for the lowest fluences, we expect a solid-solid transition, as the interface stays steep (Figure S2 of the Supporting Information).
AIMD simulations were conducted under different ionic and electronic temperatures in order to get a better understanding of the transition's dynamics observed experimentally only on ε_r. Indeed for probe wavelengths lower than 650 nm, we get a lack of sensitivity to (T_e, T_i) variations on ε_i as shown on Figure S6 (Supporting Information). This prevents us to fully investigate the fluence dependencies of the relaxation dynamics. The essential of the dynamics is due to Ge atoms : the latter shift from tetrahedral local environments in the initial amorphous state to octahedral ones as soon as excitation takes place, while the geometry of Te atoms environment does not change much. From a macroscopic point of view, this out of equilibrium state is either still an amorphous or a very viscous liquid state, yet whose properties are already very similar to the $T_i > T_m$ state. Indeed, all the configurations corresponding to the evolution of amorphous GeTe after excitation, feature the same characteristic angles, bond lengths, and VDOS.
Comparison with the AIMD simulations lead us to the following scenario : we start with an amorphous GeTe sample, in which Ge atoms are predominantly in tetrahedral local environments. The excitation induced by the 26-fs pump laser triggers the switching towards octahedral sites. In less than 300 fs, we reach an out of equilibrium state whose structure and properties are very similar to the liquid phase of GeTe. Afterwards, lattice temperature rises due to electron-phonon coupling, then reaches the melting temperature. While the structure does not change much on a local scale, the propagation of this seemingly liquid phase induces a shrinkage of the sample. Therefore, while on the sub-100 fs timescale, the switching to an amorphous excited state is "non-thermal" and driven by the bond softening, for the high fluences a thermal melting takes places on a longer timescale. This process is not without recalling of the ovonic switching phenomenon, but triggered optically in our case.

Experimental Section

Thin film preparation: All amorphous GeTe thin films were deposited in industrial 200 mm cluster tools by means of RF magnetron sputtering of a pure GeTe target under Ar atmosphere. The films were deposited on 100 mm Si (100) substrates that are well suited to be used as targets for FDI experiments. The sputtering conditions were optimized in order to achieve amorphous GeTe films with high density and excellent uniformity over the whole surface of the Si substrates as we verified by X-ray reflectivity. Typical film densities of about 5.3 g/cm3 were obtained by using an Ar flow of 20 sccm and a constant pressure of about 1E-3 mbar. The thickness of the GeTe films was fixed to 500 nm. Immediatly after deposition, half of the films were capped in situ by sputtering of a 10 nm-thick SiN layer in order to both prevent chalcogenide films' surface oxidation and enable later the formation of wrinkle patterns. All films were kept in a vacuum chamber to avoid any possible oxydation. The film thicknesses and compositions were controlled by spectroscopic ellipsometry and wavelength dispersive x-ray fluorescence (WDXRF). The atomic composition of the films was Ge∼52Te∼48 i.e. with a slight Ge excess from the GeTe composition of the target as commonly observed when using sputtering deposition process. Besides, the raw spectroscopic ellipsometry data acquired in the 200-1700 nm range were modelled using a Cody-Lorentz model in order to extract the linear optical constants of the as-deposited GeTe films.

Frequency Domain Interferometry set-up: The FDI set-up is shown in Figure 1A. The 1kHz Ti:Sapphire laser at CELIA laboratory (Aurore) [36] delivers 26 fs FWHM duration pulses at a central wavelength of 800 nm, with an energy up to 10 mJ. This incoming beam is split in two arms corresponding to the pump and the probe. A delay line placed on the pump path allows to vary the delay between the pump and

the probe. The pump is focused by a 200 mm plano-convex lens onto the GeTe sample within a 50 µm FWHM spot diameter. In the probe arm, a non-collinear optical parametric amplifier (NOPA) converts and amplifies the initial pulse to a 532 nm, 120 fs FWHM, 10 µJ pulse. FDI being a two-probes technique, a birefringent 15 mm-thick $CaC0_3$ crystal, splits the incoming 532 mn pulse into two replicas. The calcite's thickness defines not only the delay between the two probes pulses but also the maximum time delay $\delta t = \Delta t_{max} = 8.7$ ps between the pump and the second probe pulses. A thin film polarizer keeps only the P polarization of each pulse, which is then re-distributed equally between S and P polarizations by a zero order half-wave plate. The probes pulses are reflected onto the sample with an incident angle of 45°, then sent into a Fastie-Ebert spectrometer before being imaged on a CCD detector. The spectral interference patterns of the S and P polarizations are measured simultaneously for each Δt thanks to a Wollaston prism spatially separating each polarization before the CCD camera. The sample is fixed on a large rotating holder placed in a vacuum chamber, allowing to refresh the irradiated area at the kHz repetition rate. Each FDI spectrum is averaged over 1 second (1000 pulses). As the pump pulse has a Gaussian shape, we selected only few horizontal lines in the interferograms, corresponding to the maximum contribution in the intensity profile. As a result the extracted data corresponds to a given fluence, and not an averaged value over the whole Gaussian profile.
In order to have a better resolution as well as to get rid of any unwanted effect that laser irradiation might have, the results are normalized : we acquire first a spectrum with the pump-off, which will be used as a reference then we acquire a second spectrum with the pump pulse impinging on the sample.

Ab-initio simulations: Born-Oppenheimer DFT molecular simulations were performed using the Vienna Ab Initio Simulation Package [64] with Projector Augmented Wave potentials [65,66] and Generalized Gradient Approximation-Perdew-Burke-Ernzerhof exchange correlation functional [67]. Final atomic configurations result from a two-step process. First, a melt-quench approach was used to obtain the initial amorphous GeTe configuration. To generate a large proportion of homopolar bonds, 216 atoms SiTe compound was melt-quenched (3000 K → 1000 K → 600 K → 300 K in 100 ps), then Si atoms were replaced by Ge atoms before annealing, see supplementary method 1 in Reference [30]. Additional 30 to 40 ps of MD simulations were required to simulate the excited states, with a 3 fs time step, an energy cut-off of 175 eV for the charge density and a Nosé thermostat. Calculations were done on the gamma point. To mimic the electronic excitation of the laser as in the experiment, we applied a Fermi distribution (see **Equation 4)** with a fixed width σ for the electrons for each case.

$$f\left(\frac{\epsilon-\mu}{\sigma}\right) = \frac{1}{1+e^{\frac{\epsilon-\mu}{\sigma}}} \tag{4}$$

with ϵ the energy and μ the chemical potential. σ can therefore been interpreted as the electronic temperature T_e. σ was varied from 0.001 eV ("non excited") to 1.0 eV and the ionic temperature from 300 K to 1100 K.

Supporting Information

Supporting Information is available from the Wiley Online Library or from the author.

Acknowledgements

I.P. and J.G are grateful to the ANR (CASTORS project ANR-13-JS04-0002).J.-Y.R. and P. N. acknowledge the collaborative convention between CEA-LETI and FRS-FNRS. J.-Y.R. and P. M. acknowledge computational resources provided by the CECI funded by the F.R.S.-FNRS under Grant No. 2.5020.11 and the Tier-1 supercomputer of the Fédération Wallonie-Bruxelles, infrastructure funded by the Walloon Region under grant agreement n°1117545.

References

[1] S. R. Ovshinsky, *Physical Review Letters* **1968**, *21*, 20 1450.

[2] P. Noé, A. Verdy, F. d'Acapito, J.-B. Dory, M. Bernard, G. Navarro, J.-B. Jager, J. Gaudin, J.-Y. Raty, *Science Advances* **2020**, *6*, 9 eaay2830.

[3] M. Wuttig, N. Yamada, *Nature Materials* **2007**, *6*, 11 824.

[4] N. Yamada, *physica status solidi (b)* **2012**, *249*, 10 1837.

[5] J. Choe, Intel 3D XPoint Memory Die Removed from Intel Optane^{TM} PCM (Phase Change Memory), **2017**.

[6] P. Noé, C. Vallée, F. Hippert, F. Fillot, J.-Y. Raty, *Semiconductor Science and Technology* **2018**, *33*, 1 013002.

[7] G. W. Burr, R. S. Shenoy, K. Virwani, P. Narayanan, A. Padilla, B. Kurdi, H. Hwang, *Journal of Vacuum Science & Technology B, Nanotechnology and Microelectronics: Materials, Processing, Measurement, and Phenomena* **2014**, *32*, 4 040802.

[8] C. Kügeler, M. Meier, R. Rosezin, S. Gilles, R. Waser, *Solid-State Electronics* **2009**, *53*, 12 1287.

[9] W. Zhang, R. Mazzarello, M. Wuttig, E. Ma, *Nature Reviews Materials* **2019**, *4*, 3 150.

[10] W. Wełnic, A. Pamungkas, R. Detemple, C. Steimer, S. Blügel, M. Wuttig, *Nature Materials* **2006**, *5*, 1 56.

[11] K. S. Andrikopoulos, S. N. Yannopoulos, G. A. Voyiatzis, A. V. Kolobov, M. Ribes, J. Tominaga, *Journal of Physics: Condensed Matter* **2006**, *18*, 3 965.

[12] P. Zalden, M. J. Shu, F. Chen, X. Wu, Y. Zhu, H. Wen, S. Johnston, Z.-X. Shen, P. Landreman, M. Brongersma, S. W. Fong, H.-S. P. Wong, M.-J. Sher, P. Jost, M. Kaes, M. Salinga, A. von Hoegen, M. Wuttig, A. M. Lindenberg, *Physical Review Letters* **2016**, *117*, 6 067601.

[13] A. Pawbake, C. Bellin, L. Paulatto, K. Béneut, J. Biscaras, C. Narayana, D. J. Late, A. Shukla, *Physical Review Letters* **2019**, *122*, 14 145701.

[14] C. Bellin, A. Pawbake, L. Paulatto, K. Béneut, J. Biscaras, C. Narayana, A. Polian, D. J. Late, A. Shukla, *Physical Review Letters* **2020**, *125*, 14 145301.

[15] M. Behrens, A. Lotnyk, J. W. Gerlach, M. Ehrhardt, P. Lorenz, B. Rauschenbach, *ACS Appl. Mater. Interfaces* **2019**, *11*, 44 41544.

[16] H. Tanimura, S. Watanabe, T. Ichitsubo, *Advanced Functional Materials* **2020**, *n/a*, n/a 2002821.

[17] L. Waldecker, T. A. Miller, M. Rudé, R. Bertoni, J. Osmond, V. Pruneri, R. E. Simpson, R. Ernstorfer, S. Wall, *Nature Materials* **2015**, *14*, 10 991.

[18] P. Zalden, F. Quirin, M. Schumacher, J. Siegel, S. Wei, A. Koc, M. Nicoul, M. Trigo, P. Andreasson, H. Enquist, M. J. Shu, T. Pardini, M. Chollet, D. Zhu, H. Lemke, I. Ronneberger, J. Larsson, A. M. Lindenberg, H. E. Fischer, S. Hau-Riege, D. A. Reis, R. Mazzarello, M. Wuttig, K. Sokolowski-Tinten, *Science* **2019**, *364*, 6445 1062.

[19] S. K. Sundaram, E. Mazur, *Nature Materials* **2002**, *1*, 4 217.

[20] E. Matsubara, S. Okada, T. Ichitsubo, T. Kawaguchi, A. Hirata, P. F. Guan, K. Tokuda, K. Tanimura, T. Matsunaga, M. W. Chen, N. Yamada, *Physical Review Letters* **2016**, *117*, 13.

[21] T. A. Miller, M. Rudé, V. Pruneri, S. Wall, *Physical Review B* **2016**, *94*, 2 024301.

[22] T. Kawaguchi, K. Tokuda, S. Okada, M. Yabashi, T. Ichitsubo, N. Yamada, E. Matsubara, *Physical Review B* **2020**, *101*, 6 060302.

[23] K. Sokolowski-Tinten, J. Solis, J. Bialkowski, J. Siegel, C. N. Afonso, D. von der Linde, *Physical Review Letters* **1998**, *81*, 17 3679.

[24] J. P. Callan, A. M.-T. Kim, C. A. D. Roeser, E. Mazur, J. Solis, J. Siegel, C. N. Afonso, J. C. G. de Sande, *Physical Review Letters* **2001**, *86*, 16 3650.

[25] J.-Y. Raty, M. Schumacher, P. Golub, V. L. Deringer, C. Gatti, M. Wuttig, *Advanced Materials* **2019**, *31*, 3 1806280.

[26] M. Wuttig, V. L. Deringer, X. Gonze, C. Bichara, J.-Y. Raty, *Advanced Materials* **2018**, *30*, 51 1803777.

[27] M. Zhu, O. Cojocaru-Mirédin, A. M. Mio, J. Keutgen, M. Küpers, Y. Yu, J.-Y. Cho, R. Dronskowski, M. Wuttig, *Advanced Materials* **2018**, *30*, 18 1706735.

[28] A. V. Kolobov, P. Fons, J. Tominaga, *physica status solidi (b)* **2014**, *251*, 7 1297.

[29] J. Akola, J. Larrucea, R. O. Jones, *Physical Review B* **2011**, *83*, 9.

[30] J. Y. Raty, W. Zhang, J. Luckas, C. Chen, R. Mazzarello, C. Bichara, M. Wuttig, *Nature Communications* **2015**, *6*, 1 7467.

[31] M. Micoulaut, A. Piarristeguy, H. Flores-Ruiz, A. Pradel, *Physical Review B* **2017**, *96*, 18 184204.

[32] M. Hong, J. Zou, Z.-G. Chen, *Advanced Materials* **2019**, *31*, 14 1807071.

[33] C. Rinaldi, J. C. Rojas-Sánchez, R. N. Wang, Y. Fu, S. Oyarzun, L. Vila, S. Bertoli, M. Asa, L. Baldrati, M. Cantoni, J.-M. George, R. Calarco, A. Fert, R. Bertacco, *APL Materials* **2016**, *4*, 3 032501.

[34] G. Bruns, P. Merkelbach, C. Schlockermann, M. Salinga, M. Wuttig, T. D. Happ, J. B. Philipp, M. Kund, *Applied Physics Letters* **2009**, *95*, 4 043108.

[35] J. P. Geindre, A. Mysyrowicz, A. D. Santos, P. Audebert, A. Rousse, G. Hamoniaux, A. Antonetti, F. Falliès, J. C. Gauthier, *Optics Letters* **1994**, *19*, 23 1997.

[36] N. Fedorov, S. Beaulieu, A. Belsky, V. Blanchet, R. Bouillaud, M. De Anda Villa, A. Filippov, C. Fourment, J. Gaudin, R. E. Grisenti, E. Lamour, A. Lévy, S. Macé, Y. Mairesse, P. Martin, P. Martinez, P. Noé, I. Papagiannouli, M. Patanen, S. Petit, D. Vernhet, K. Veyrinas, D. Descamps, *Review of Scientific Instruments* **2020**, *91*, 10 105104.

[37] C. Fourment, B. Chimier, F. Deneuville, D. Descamps, F. Dorchies, G. Duchateau, M.-C. Nadeau, S. Petit, *Physical Review B* **2018**, *98*, 15.

[38] F. Deneuville, B. Chimier, D. Descamps, F. Dorchies, S. Hulin, S. Petit, O. Peyrusse, J. J. Santos, C. Fourment, *Applied Physics Letters* **2013**, *102*, 19 194104.

[39] K. V. Mitrofanov, P. Fons, K. Makino, R. Terashima, T. Shimada, A. V. Kolobov, J. Tominaga, V. Bragaglia, A. Giussani, R. Calarco, H. Riechert, T. Sato, T. Katayama, K. Ogawa, T. Togashi, M. Yabashi, S. Wall, D. Brewe, M. Hase, *Scientific Reports* **2016**, *6*, 1 20633.

[40] P. Martinez, I. Papagiannouli, D. Descamps, S. Petit, J. Marthelot, A. Lévy, B. Fabre, J.-B. Dory, N. Bernier, J.-Y. Raty, P. Noé, J. Gaudin, *Advanced Materials* **2020**, *32*, 38 2003032.

[41] K. Hirota, K. Nagino, G. Ohbayashi, *Journal of Applied Physics* **1997**, *82*, 1 65.

[42] A. V. Kolobov, P. Fons, A. I. Frenkel, A. L. Ankudinov, J. Tominaga, T. Uruga, *Nature Materials* **2004**, *3*, 10 703.

[43] J. Akola, R. O. Jones, *Physical Review B* **2007**, *76*, 23 235201.

[44] P. Noé, C. Sabbione, N. Castellani, G. Veux, G. Navarro, V. Sousa, F. Hippert, F. d'Acapito, *Journal of Physics D: Applied Physics* **2016**, *49*, 3 035305.

[45] J.-Y. Raty, C. Otjacques, J.-P. Gaspard, C. Bichara, *Solid State Sciences* **2010**, *12*, 2 193.

[46] R. Mazzarello, S. Caravati, S. Angioletti-Uberti, M. Bernasconi, M. Parrinello, *Physical Review Letters* **2010**, *104*, 8 085503.

[47] J. Akola, R. O. Jones, *Physical Review Letters* **2008**, *100*, 20 205502.

[48] J. Y. Raty, V. Godlevsky, P. Ghosez, C. Bichara, J. P. Gaspard, J. R. Chelikowsky, *Physical Review Letters* **2000**, *85*, 9 1950.

[49] J. Y. Raty, V. V. Godlevsky, J. P. Gaspard, C. Bichara, M. Bionducci, R. Bellissent, R. Céolin, J. R. Chelikowsky, P. Ghosez, *Physical Review B* **2002**, *65*, 11 115205.

[50] G. C. Sosso, J. Behler, M. Bernasconi, *physica status solidi (a)* **2016**, *213*, 2 329.

[51] H. Weber, M. Schumacher, P. Jóvári, Y. Tsuchiya, W. Skrotzki, R. Mazzarello, I. Kaban, *Physical Review B* **2017**, *96*, 5 054204.

[52] S. Gabardi, S. Caravati, G. C. Sosso, J. Behler, M. Bernasconi, *Physical Review B* **2015**, *92*, 5 054201.

[53] Y. Maeda, M. Wakagi, *Japanese Journal of Applied Physics* **1991**, *30*, Part 1, No. 1 101.

[54] J. R. Stellhorn, S. Hosokawa, W.-C. Pilgrim, N. Blanc, N. Boudet, H. Tajiri, S. Kohara, *physica status solidi (b)* **2016**, *253*, 6 1038.

[55] P. Jóvári, A. Piarristeguy, R. Escalier, I. Kaban, J. Bednarčik, A. Pradel, *Journal of Physics: Condensed Matter* **2013**, *25*, 19 195401.

[56] G. E. Ghezzi, J. Y. Raty, S. Maitrejean, A. Roule, E. Elkaim, F. Hippert, *Applied Physics Letters* **2011**, *99*, 15 151906.

[57] S. Kohara, K. Kato, S. Kimura, H. Tanaka, T. Usuki, K. Suzuya, H. Tanaka, Y. Moritomo, T. Matsunaga, N. Yamada, Y. Tanaka, H. Suematsu, M. Takata, *Applied Physics Letters* **2006**, *89*, 20 201910.

[58] A. V. Kolobov, P. Fons, J. Tominaga, *Physical Review B* **2013**, *87*, 15 155204.

[59] M. Inui, A. Koura, Y. Kajihara, S. Hosokawa, A. Chiba, K. Kimura, F. Shimojo, S. Tsutsui, A. Q. R. Baron, *Physical Review B* **2018**, *97*, 17 174203.

[60] J.-P. Gaspard, A. Pellegatti, F. Marinelli, C. Bichara, *Philisophical Magazine B* **1998**, *77*, 3 727.

[61] M. Wuttig, *physica status solidi (b)* **2012**, *249*, 10 1843.

[62] Y. Tsuchiya, *Thermochimica Acta* **1998**, *314*, 1 275.

[63] G. Lucovsky, R. M. White, *Physical Review B* **1973**, *8*, 2 660.

[64] G. Kresse, J. Hafner, *Physical Review B* **1994**, *49*, 20 14251.

[65] G. Kresse, D. Joubert, *Physical Review B* **1999**, *59*, 3 1758.

[66] P. E. Blöchl, *Physical Review B* **1994**, *50*, 24 17953.

[67] J. P. Perdew, K. Burke, Y. Wang, *Physical Review B* **1996**, *54*, 23 16533.

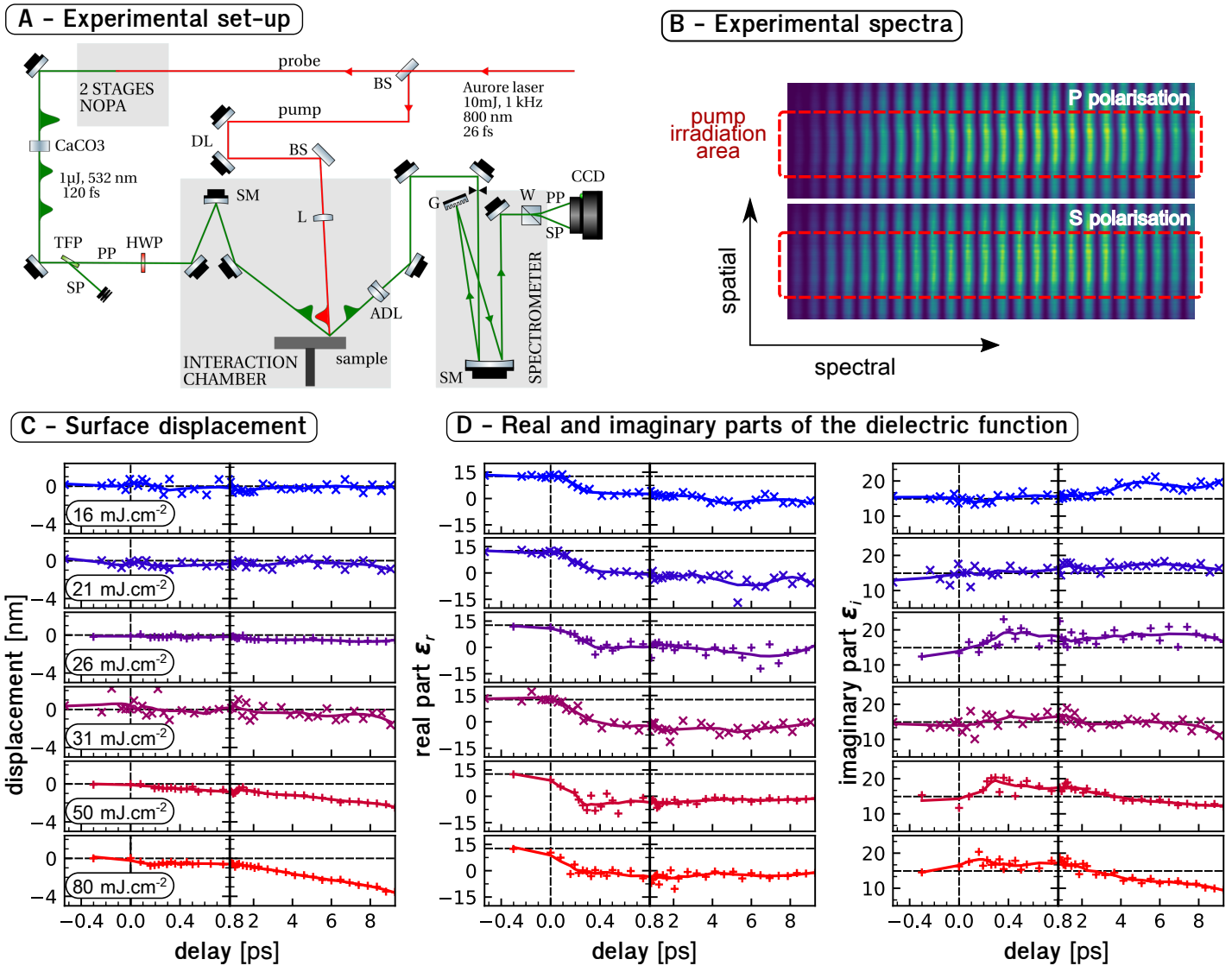

Figure 1: A) FDI set-up. BS : beamsplitter, NOPA : non collinear optical parametric amplifier, $CaCO_3$: calcite crystal, DL : delay line, SM : spherical mirror, L : lens, ADL : achromatic doublet, TFP : thin film polarizer, G : grating W: Wollaston prism, SP : S polarization, PP : P polarization, HWP : zero order half wave plate. B) FDI Spectra in P (top) and S (bottom) polarizations for $\Delta t = 8.5$ ps delay and a pump of $80\,\mathrm{mJ/cm^2}$ C) Displacement of the surface. ("x" : SiN capped and "+" : uncapped amorphous GeTe samples, solid lines are guides to the eyes) D) Dielectric function (horizontal dotted lines = ε_{cold} = 12.66 + 14.93 i at 532 nm, determined by preliminary ellipsometry measurements at 293 K.)

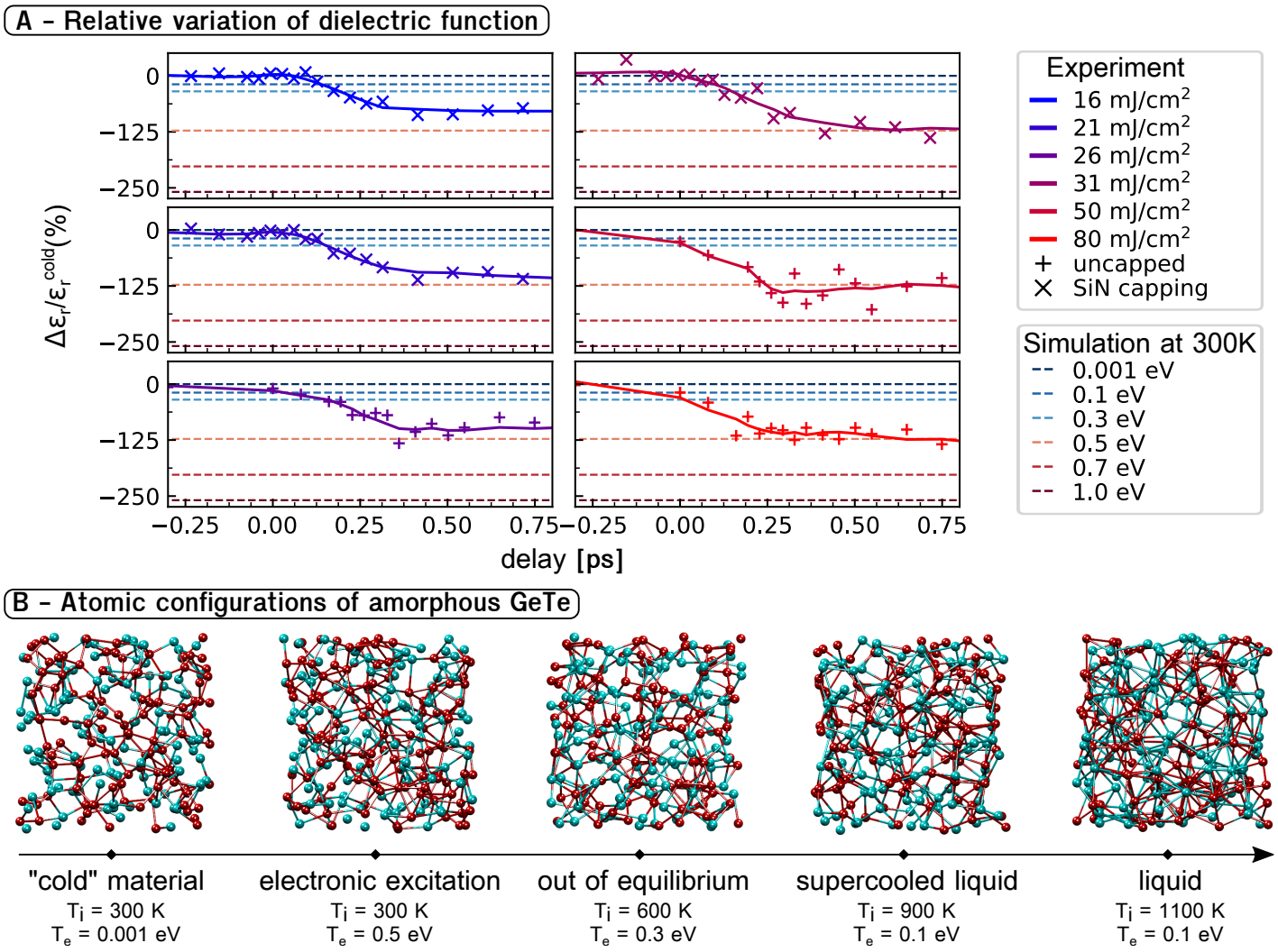

Figure 2: A) Comparison of the dielectric function from FDI measurement and simulation. Data from the experiment are represented by "x" and "+" (solid lines = guides to the eyes). Horizontal dotted lines are the results from simulation at T_i = 300 K for different T_e. From this we infer that $T_e \sim 0.5$ eV corresponds to the electronic excitation induced by laser. ε^{cold} corresponds to the experimental value measured by ellipsometry before laser irradiation, and to the case (T_i = 300 K, T_e=0.001 eV) for the simulations. B) Atomic configurations for different (T_e, T_i) cases. Blue : Te atoms, Red : Ge atoms (cut-off radii for bonds representations are presented in Table 2).

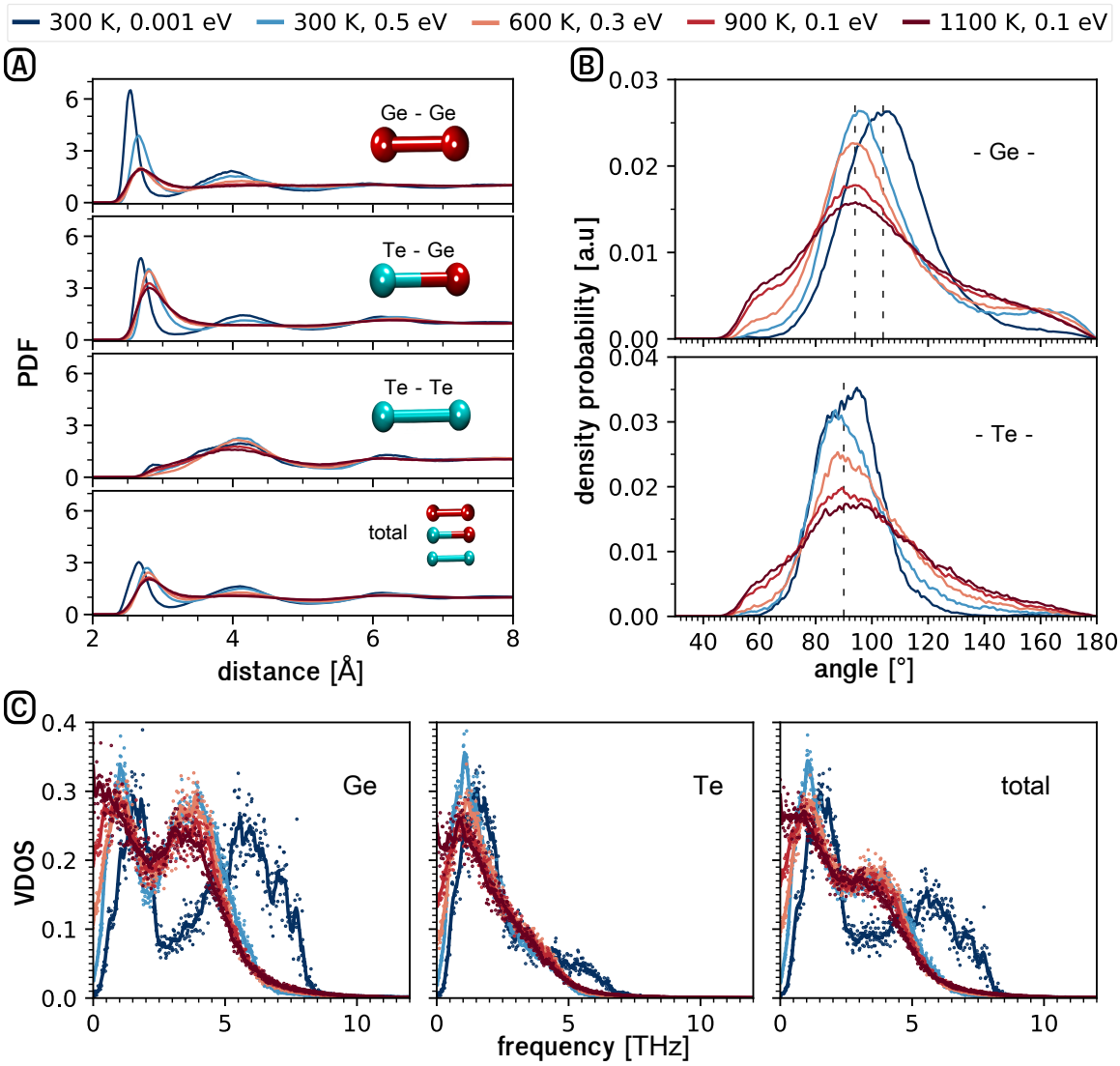

Figure 3: A) Pair distribution function. B) Angular distribution C) Vibrational Density of States (solid lines are guides to the eyes)

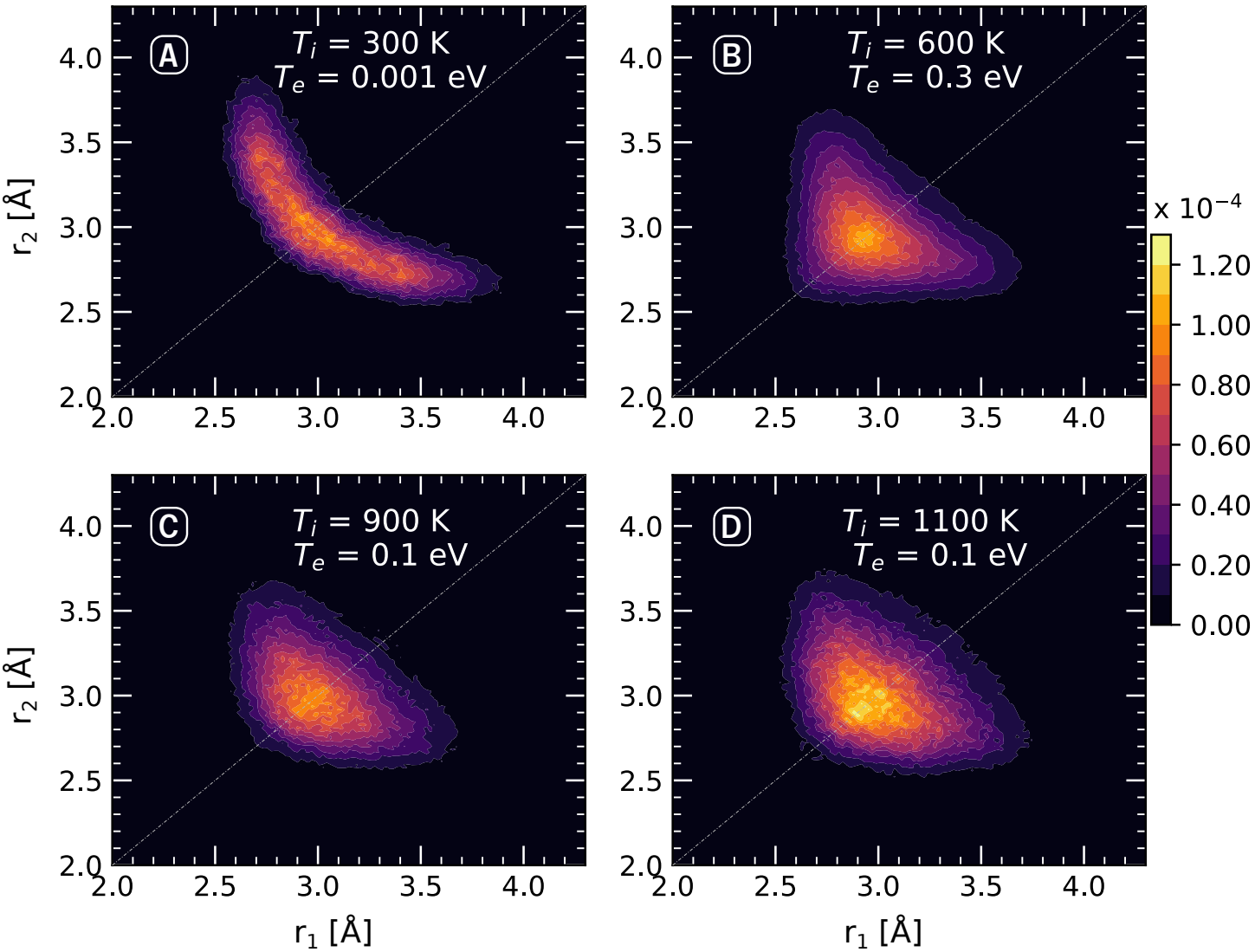

Figure 4: Te-Ge-Te Angular Limited Three-Body Correlation (ALTBC) with a deviation of interbond angle of 25°. A) Cold state. B) Out of equilibrium state. C) Supercooled state. D) Liquid state.